Postprint of: Kabir A., Lemieszek B., Varenik M., Buratto Tinti V., Molin S., Lubomirsky I., Esposito V., Kern F., Enhanced Mechanical and Electromechanical Properties of Compositionally Complex Zirconia $Zr_{1-x}(Gd_{1/5}Pr_{1/5}Nd_{1/5}Sm_{1/5}Y_{1/5})_xO_{2-\delta}$ Ceramics, ACS Applied Materials & Interfaces, Vol. 16, Iss. 10 (2024), pp. 12765-12772, DOI: 10.1021/acsami.3c17501

Enhanced mechanical and electromechanical properties of compositionally complex zirconia $Zr_{1-x}(Gd_{1/5}Pr_{1/5}Nd_{1/5}Sm_{1/5}Y_{1/5})_xO_{2-\delta}$ ceramics

Ahsanul Kabir[a]*, Bartłomiej Lemieszek[b], Maxim Varenik[c], Victor Buratto Tinti[d], Sebastian Molin[b], Igor Lubomirsky[c], Vincenzo Esposito[d], and Frank Kern[a]

[a.] University of Stuttgart, Institute for Manufacturing Technology of Ceramic Components and Composites, 70569 Stuttgart, Germany

[b.] Advanced Materials Center, Faculty of Electronics, Telecommunications, and Informatics, Gdańsk University of Technology, ul. G. Narutowicza 11/12, 80-233 Gdańsk, Poland

[c.] Department of Molecular Chemistry and Materials Science, Weizmann Institute of Science, Rehovot 7610001, Israel

[d.] Department of Energy Conversion and Storage, Technical University of Denmark, 2800 Kgs. Lyngby, Denmark

E-mail: ahsanul.kabir@ ifkb.uni-stuttgart.de

Abstract

Compositionally complex oxides (CCOs) or high-entropy oxides (HEOs) are new multi-element oxides with unexplored physical and functional properties. In this work, we report fluorite structure derived compositionally complex zirconia with composition $Zr_{1-x}(Gd_{1/5}Pr_{1/5}Nd_{1/5}Sm_{1/5}Y_{1/5})_xO_{2-\delta}$ (x = 0.1 and 0.2) synthesized in solid-state reaction route and sintered via hot pressing at 1350 °C. We explore the evolution of these oxides' structural, microstructural, mechanical, electrical, and electromechanical properties regarding phase separation and sintering mechanisms. Highly dense ceramics are achieved by bimodal mass diffusion, composing nanometric tetragonal and micrometric cubic grains microstructure. The material exhibits an anomalously large electrostriction response exceeding the M_{33} value of 10^{-17} m^2/V^2 at room temperatures and viscoelastic properties of primary creep in nanoindentation measurement under fast loading. These findings are strikingly similar to those reported for doped ceria and bismuth oxide derivates, highlighting the presence of a large concentration of point defects linked to structural distortion and anelastic behavior are characteristics of nonclassical ionic electrostrictors.

Keywords: high entropy oxides; zirconia; ionic conductivity, electrostriction; microstructure

Introduction

In recent years, an entirely different family of a material class has attracted substantial attention in the ceramics science community, known as compositionally complex oxides (CCOs) or high entropy oxides (HEOs), and are mainly derived from the concept of "high entropy" from high entropy alloys or multicomponent alloys [123]. These are single-phase metal oxides consisting of five or more different cations in an equal or near equal atomic percent, *i.e.* the entropy of mixing ΔS_{mix} higher than ≈ 1.5 kB/f.u that are integrated on the same crystallographic lattice site [45]. HEOs have a large number of tuning spaces in composition and crystal structure, offering new perspectives for tailoring their materials properties [67]. In 2015 Rost et al. synthesized the first HEOs $(Mg_{0.2}Co_{0.2}Ni_{0.2}Cu_{0.2}Zn_{0.2})O$, with a rock-salt structure that shows a reversible mixing/demixing behavior upon heating and cooling, respectively, and is truly entropy stabilized [1]. Following this seminal work, the realm of HEOs was explored in different oxide systems, including fluorites [8], spinels [9], perovskites [10], rutiles [11], pyrochlores [12], and beyond. Compared to binary or doped oxides, improved properties such as high ionic conductivity, low thermal conductivity, colossal dielectric constant, improved thermoelectric figure of merit, etc., are often reported in the literature [111314].

Fluorite oxide is an imperative type of structural/functional ceramics material. It has a plethora of technical applications, including solid-state ionic conductors, thermal barrier coatings, gas sensors, oxygen storage capacitors, biomarkers, memristors, and catalysts [151617]. Most conventional fluorites are based on ceria, zirconia, or hafnia and are usually doped/stabilized with rare earth oxides (RE_2O_3) and alkaline oxides such as MgO and CaO [18]. They hold properties like high ionic conductivity (0.01 S/cm at 600 °C [16]), low thermal conductivity (1.5 $Wm^{-1}K^{-1}$, at 1000 °C [19]), high-temperature phase stability, high hardness (12.4 GPa [20]) and fracture toughness (10 $MPa*m^{1/2}$ [20]). Moreover, unconventional mechanical (room temperature creep) and electromechanical characteristics have been observed in oxygen-defective fluorites such as $CeO_{2-\delta}$ and δ-phase-$Bi_2O_{3-\delta}$, which have newly advanced [21222324]. These properties were associated with the presence of charge-compensating oxygen vacancies in the fluorites, mainly dopant-controlled [1825]. In many HEO systems, high-entropy fluorite-structured oxides (HEFOs) have drawn much attention for their compositional design and modified performance [26]. Gild et al. fabricated a series of bulk single-phase high-entropy fluorite oxides HEFOs, e.g.,

$(Zr_{0.2}Ce_{0.2}Hf_{0.2})(Y_{0.2}Gd_{0.2})O_2$, with equimolar ZrO_2-CeO_2-HfO_2 as the matrix with lower thermal and electrical conductivity than YSZ [8]. A similar result was also reported by Chen et al. with HEFOs of $(Zr_{0.2}Hf_{0.2}Ce_{0.2})(Sn_{0.2}Ti_{0.2})O_{2-\delta}$ [27]. Wright et al. explored non-equimolar $(Zr_{1/3}Hf_{1/3}Ce_{1/3})_{1-x}(Y_{1/2}X_{1/2})_xO_{2-x/2}$ based compositions where X = Yb, Ca, and Gd and investigated mechanical and thermal conductivities [28]. M. Zhu and coworkers fabricated a series of multielement doped high-entropy ceria $Ce_{1-x}(Dy_{1/5}Sm_{1/5}Er_{1/5}Y_{1/5}Gd_{1/5})_xO_{2-\delta}$ with single phase fluorite structure, which shows ionic conductivity of 1.05×10^{-3} S/cm at 500 °C [29]. Spiridigliozzi et al. synthesized $Ce_{0.2}Zr_{0.2}Y_{0.2}Gd_{0.2}La_{0.2}O_{2-\delta}$ [30] and investigated densification behavior at ultrafast high-temperature sintering (UHS) [31]. Similarly, F. Ye and co-workers investigated the sintering behavior of 5 multicomponent rare earth hafnate with defective fluorite structure by the UHS method [32]. Rare earth-based HEFO powders containing up to seven equiatomic elements, i.e., Ce, La, Nd, Pr, Sm, Y, and Gd, were also synthesized by Djenadic and coworkers [3334]. These authors also suggested that not only the entropy effect but also element type (valence, cation size), presence of Ce^{4+} as parent structure, synthesis method (equilibrium, non-equilibrium), and crystallite size are also important factors to stabilize the desired single-phase structure in HEFOs. Since there is a limited number of tetravalent cations, most of the HEFOs synthesized so far are non-stochiometric oxides with oxygen vacancies [35]. It is worth mentioning that the terms "high entropy", "entropy stabilized" and "compositionally complex" are alternatively used in the literature although they are not synonymous [36]. Materials having a high number of elements residing on one or more sublattices are considered compositionally complex oxides (CCOs), which also encompass non-equimolar and medium entropic compositions [28]. The HEO (a subset of CCO) refers to materials in which high configurational entropy has some effect on phase stabilization but it is not inevitably dominant over enthalpy [436]. On the other hand, entropy-stabilized oxides (ESOs) are a subset of HEO with a strict thermodynamic definition. ESO requires both high configurational entropy and positive enthalpy of formation ($+\Delta H$) so that entropy drives thermodynamic stability [3037].

Inspired by the above-mentioned literature works, herein, we synthesize fluorite-structure derived multi-element doped compositionally complex zirconia (CCZ) ceramics and investigate their structural, microstructural, electrical, mechanical, and electromechanical properties. Two compositions were successfully synthesized namely, $((Zr_{0.9}Gd_{0.02}Pr_{0.02}Nd_{0.02}Sm_{0.02}Y_{0.02})O_{2-\delta}$: CCZ-10 and $((Zr_{0.8}Gd_{0.04}Pr_{0.04}Nd_{0.04}Sm_{0.04}Y_{0.04})O_{2-\delta}$: CCZ-20). It is worth mentioning that

praseodymium under reducing conditions is prevalently trivalent. Yet, the unstable tetravalent structure can introduce unexpected dissociative effects with the annihilation of oxygen vacancies [38]. Although most of the reported HEFO compound in the literature has higher oxygen vacancy concentrations than typical doped or non-stoichiometric binary rare oxides, we kept the oxygen vacancy concentration of ≤ 2.5 % (δ = 0.1). Various literature reports that 10-20 mol% dopant concentration meaningfully impacts the electrical, mechanical, and electrostriction effect in the fluorite structure compounds, *e.g.* doped ceria [213940]. High dopant concentrations modify the energy landscape of the lattice site and migration barriers, forming solid solutions that resemble RE_2O_3 and superstructure with dopant-oxygen vacancy complexes [4142]. This thermodynamic effect challenges the conventional design rule for fluorite-structure oxides.

Experimental work

The starting basis powders for this study were monoclinic zirconia (UEP, DKKK Japan, S_{BET} = 23 m²/g, d_{50} = 250 nm). All these rare earth oxides ($PrO_{1.83}$, $NdO_{1.5}$, $SmO_{1.5}$, $GdO_{1.5}$, and $YO_{1.5}$) have 99.9% purity (chemPur, Karlsruhe, Germany). The powders were dispersed in a stoichiometric ratio in 2-propanol and milled in a high-speed attrition mill (1000 rpm) for 4 hours using zirconia milling balls (Ø = 2 mm). Then, the dispersion was sieved through a 100 μm screen to remove milling debris and dried at 85 °C for 12 hours. The dried powder was crushed and screened through a 100 μm mesh. Afterward, the powder was consolidated by hot pressing (FCT Anlagenbau, Germany) in graphite dies of 40 mm diameter under vacuum at 1350 °C for 1 hour at a uniaxial pressure of 60 MPa. The resultant CCZ-10 and CCZ-20 pellets were mirror polished and subsequently cut into a bar shape of dimensions 10 x 5 x 1.3 mm^3. The bulk density was measured by the Archimedes method using distilled water as a medium. The crystalline phase purity was analyzed by X-ray diffraction (XRD, Philips PANalytical, Germany), containing CuKα1 radiation (λ = 0.15418 nm) within the 2θ range from 20-80° and Raman spectroscopy (Renishaw InVia Reflex, UK) equipped with an equipped with a 40 mW, 532 nm Ar+ laser. The microstructure of the samples was examined by high-resolution scanning electron microscopy (SEM, Zeiss Gemini, Germany). The grain size was estimated by the linear intercept method, multiplying with a correction factor of 1.57 [43]. The mechanical properties, including Young's modulus, 4pt bending strength, Vickers hardness HV10, and fracture toughness were carried out following a standard protocol explained in detail elsewhere [44]. The creep was measured from the nanoindentation measurements, as described in Ref [45]. A maximum

load of 150 mN was applied using a trapezoidal load-hold (20 s)-unload cycle at a constant loading/unloading rate of 15 mN/s. The electromechanical properties were measured at room temperature using a proximity sensor. A sinusoidal electric field was applied at different frequencies, and the resulting electrostrictive displacements were determined at the second harmonic to the oscillation amplitude. The electrical properties are measured by AC impedance spectroscopy, using a Novo control frequency analyzer at 250-500 °C with a frequency range of 3 MHz to 50 mHz under a bias perturbation amplitude of 25 mV in the air. Platinium (Pt) paste was brushed on the parallel face of the sample and then fired at 700 °C for 1 hour. Gold mesh and Pt wire were used as a current collector and current leads, respectively. Before the measurement, the sample was held for 20 min at the target temperature, ensuring thermal equilibrium. The impedance data were fitted with an equivalent circuit model using the ZView software.

Results and Discussion

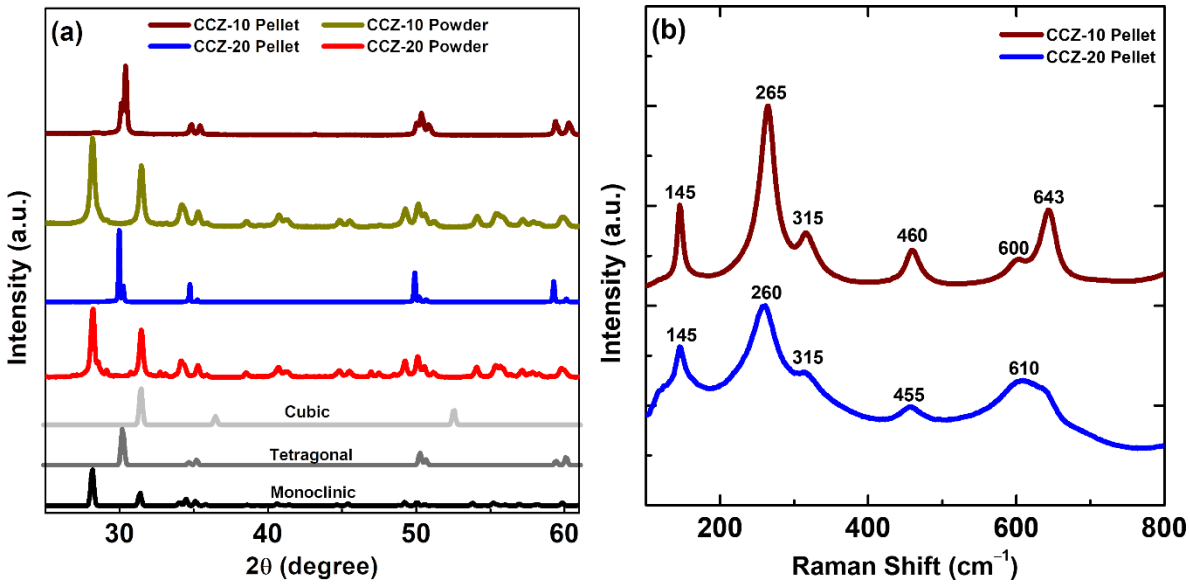

Figure 1: (a) Room-temperature XRD pattern of the starting powders (CCZ-10 and CCZ-20) and respective sintered ceramics pellets. The XRD patterns are compared with monoclinic (ICSD code 47803), tetragonal (ICSD code 123093), and cubic (ICSD code 92095) crystal structures of zirconia polymorphs. (b) Raman spectra of the sintered CCZ-ceramics (800-100 cm^{-1} wavenumber region).

Fig. 1a shows the XRD patterns of starting CCZ powders and the surface of the sintered ceramics pellets. As can be seen, powders show a typical diffraction pattern of monoclinic

zirconia, suggesting that no solid solution was formed and powders have a core-shell type configuration. However, the diffractogram of the sintered samples shows tetragonal and cubic phases and no monoclinic phase. The CCZ-20 sample has a mixture of tetragonal and cubic phases, while CCZ-10 has mainly a tetragonal phase. The crystallographic phase structure is further confirmed by Raman spectra and shown in **Fig. 1b**. According to the literature study, the tetragonal phase reveals vibrational bands located at approximately 147, 261, 318, 463, and 637 cm^{-1} [46,47,48]. The peak positions of the CCZ-10 and CCZ-20 samples are in close agreement with the literature results. The spectrum of the cubic zirconia phase was similar to that of the tetragonal, with a common peak at ~145, 260, and 460 cm^{-1}. The broad peak at 610 cm^{-1} in CCZ-20 is ascribed to the cubic phase. Gazzoli et al. reported that the cubic-zirconia phase presents a strong band between 607 and 617 cm^{-1} [46]. Similar to XRD, there were no representative peaks for the monoclinic phase, indicating that the results of the Raman and XRD analyses are consistent.

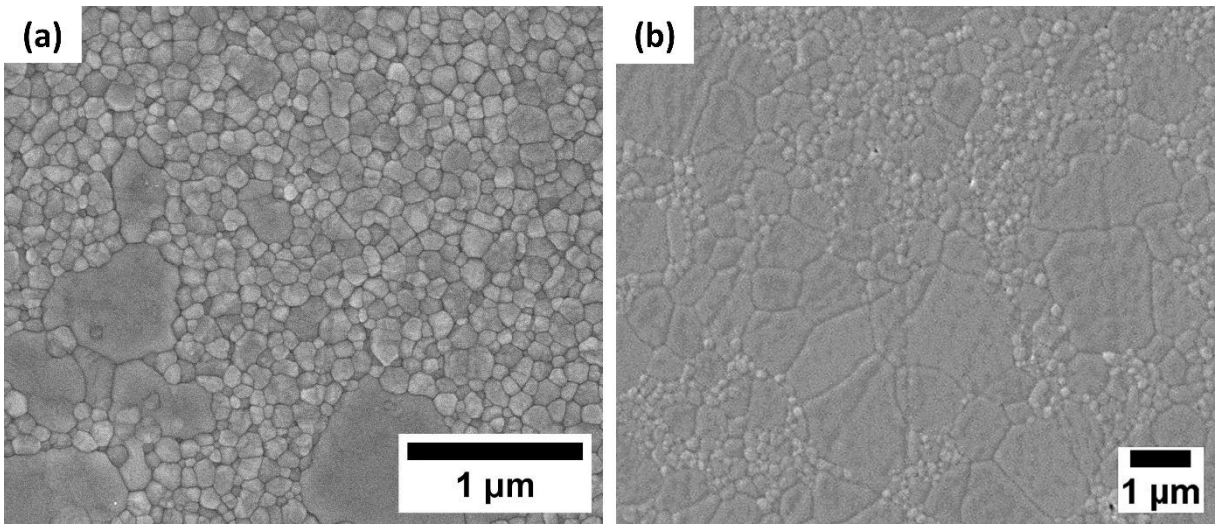

Figure 2. Polished cross-sectional scanning electron microscopy images of the thermally etched (a) CCZ-10 and (b) CCZ-20 samples, hot pressed at 1350 °C.

The materials were fully densified during sintering, exhibiting a bulk density between 6.18-6.22 g/cm^3. The high densification is further evidenced by the SEM micrograph, which is illustrated in **Fig. 2**. As apparent, the grain size distribution is bimodal, with a nanoscale tetragonal matrix and large micron-sized cubic grains. Even though five cationic elements were used, neither

sample showed any cationic segregation. The cubic grains are relatively flat, with a small residual grain boundary curvature, and the tetragonal grains are faceted. The co-existence of tetragonal and cubic phase in both materials indicates that the compositions are located in the t+c field of the zirconia/multi-rare earth oxide system which is a miscibility gap. This type of metastable microstructure is characteristically observed for low dopant contents e.g. in 3YSZ/TZP (tetragonal zirconia polycrystal) ceramics, as reported in Ref. [495051]. It was demonstrated that large grains comprise considerably higher dopant/stabilizer content than the fine matrix. The CCZ-20 sample showed a significantly higher fraction of cubic grains than the CCZ-10 sample. Such an outcome is expected due to the high stabilizer/dopant content in the former and indicates that a maximum level of entropy has been overcome in the material. The average grain size (tetragonal phase) of the CCZ-10 and CCZ-20 samples was 150 nm and 500 nm, respectively. The energy dispersive X-ray spectroscopy (EDS) elemental mapping is shown in the supplementary information (Fig. **S1-S2**).

Fig. 3a illustrates the geometry normalized impedance spectra in the form of Nyquist plots examined at 400 °C. The data was fitted by an equivalent-circuit model (shown in the inset) consisting of a resistor (R) connected in parallel with the constant-phase element (Q). Two depressed semicircles are observed in the complex impedance plane. Such depression is due to the non-ideal capacitance of the samples (CPE exponents value lower than 1). The high-frequency semicircle corresponds to bulk (intra-granular) resistance, while the intermediate frequency arc is attributed to the grain boundaries (inter-granular) resistance [52]. The low-frequency tail is associated with electrode phenomena and is irrelevant for further investigation. The low-frequency intercept of the depressed semicircle was taken as the sample resistance. The total ionic conductivity (σ) of the sample is measured using the formula $\sigma = (\frac{1}{R}\frac{t}{A})$ where R is the sample resistance, t is the thickness, and A is the electrode area. Electronic conductivity is negligible under atmospheric air. With increasing temperature, resistivity decreases and shifts to higher frequencies.

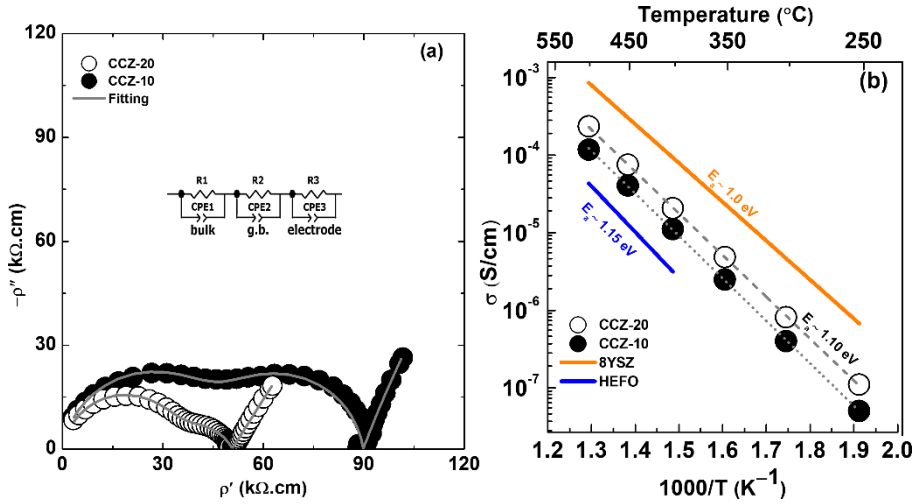

Figure 3: (a) Representation of geometry normalized Nyquist plots (ρ' vs ρ'') of CCZ ceramics, measured in atmospheric air at 400 °C. (b) The temperature-dependent Arrhenius plots of total ionic conductivity of the CCZ samples. The data is compared with the reference 8YSZ [52] and HEFO ($Hf_{0.25}Ce_{0.25}Zr_{0.25}Y_{0.125}Gd_{0.125}O_{1.875}$) samples [28].

The electrical conductivity is plotted as a function of reciprocal temperature, which follows the Arrhenius equation and is shown in **Fig. 3b,**

$$\sigma = \frac{\sigma_0}{T} exp\left(-\frac{E_a}{kT}\right)$$

(1),

where σ_0 is the pre-exponent factor (temperature-independent), k is the Boltzmann constant, and E_a is the activation energy of migrating oxygen ions. As can be seen, the measured ionic conductivity of the CCZ-20 sample is higher than the CCZ-10 compound sample throughout the investigated temperature, which could be attributed to the higher oxygen vacancy concentration and higher % of cubic phase in the former than the latter. The conductivity value is significantly lower than the 8YSZ sample, which is expected. It was demonstrated that cubic solid solutions based on zirconium dioxide show the highest conductivity. Moreover, the conductivity value is higher than HEFO, reported in Ref. [28]. This outcome is not surprising since most HEFOs have higher doping levels than the optimal amount required for zirconia-based systems. As mentioned in the introduction section, high dopant/stabilizer concentrations form dopant-oxygen vacancy clusters and RE_2O_3 solid solution which negatively impact the ionic conductivity. Both the CCZ samples have an activation energy value of ~1.10 eV, close to the value of 8YSZ.

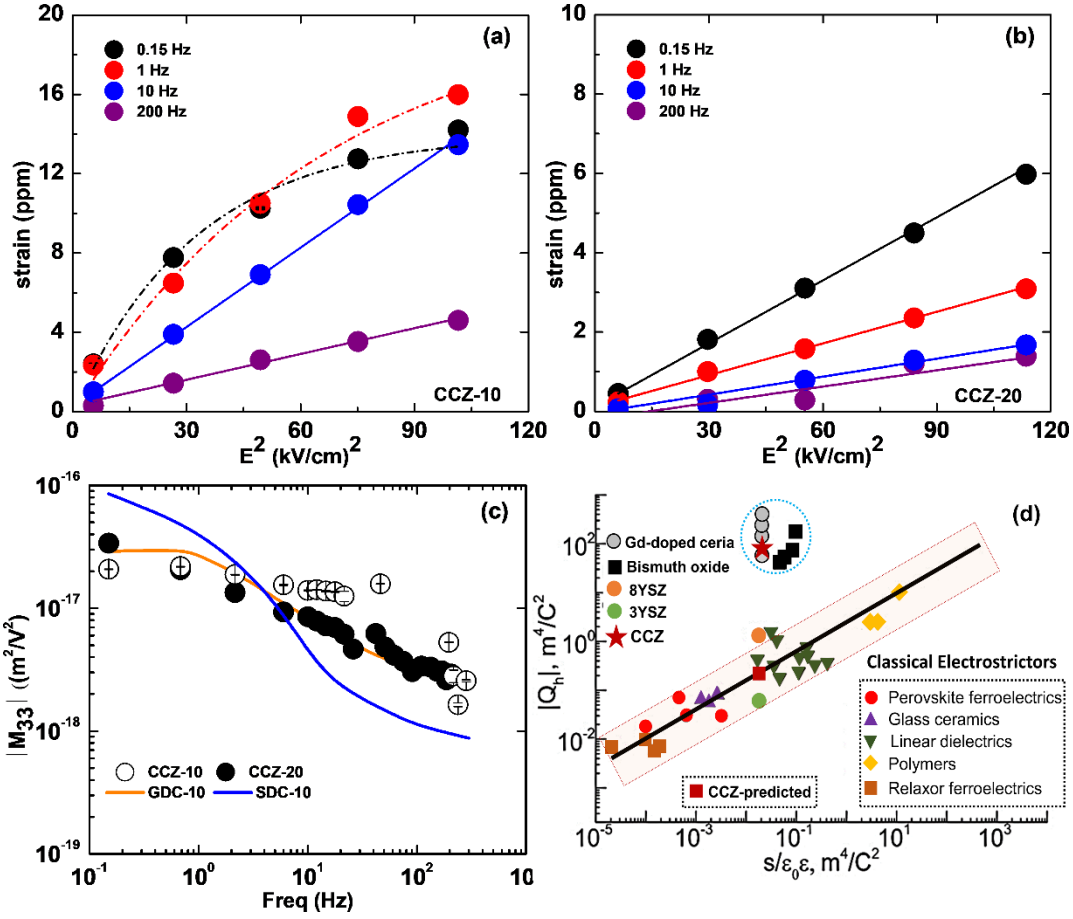

Figure 4: (a-b) Electrostrictive longitudinal strain responding to electric field square for the CCZ-10 and CCZ-20 ceramics pellet. (c) Electrostrictive strain coefficient (M_{33}) as a function of applied frequencies (0.15-300 Hz) under an electric field of 7 kV/cm, respectively. The results are compared with GDC-10 and SDC-10 samples, data taken from Ref. [21][53]. (d) Hydrostatic polarization electrostriction coefficient $|Q_h|$ as a function of the ratio of elastic compliance to the dielectric constant, the black fitted line corresponds to Newnham's empirical equation $|Q_h| \approx 2.37(s/\epsilon_0\epsilon_r)^{0.6}$. The pink area refers to the values within one order of the magnitudes of the black line. The data is taken from Ref. [545556]. Error bars show statistical ambiguity as well as instrumental precision. Error bar (Fig 4a, 4b and 4c) inside the symbol highlights that the uncertainty is lower than the size of the symbol.

The samples respond at the second harmonic of the applied electric field frequency and demonstrate characteristic electrostriction behavior. The longitudinal electrostrictive strain as a function of the electric field square is presented in **Fig. 4a-b**. The samples contracted parallel to the direction of the electric field strain and were similar to oxygen-defective cerium and bismuth

oxide-based compounds (thin films and bulk ceramics). In contrast, most ceramic electrostrictors extend along the direction of the electric field [57]. The CCZ-10 sample displays a slightly larger strain than the CCZ-20 ceramics (e.g., ~3.1 ppm for CCZ-20 and ~10.2 ppm for CCZ-10 at ~7 kV/cm and 0.1 Hz). However, the strain value shows a marked reduction with increasing frequencies in both samples. Also, in the case of the CCZ-10 sample, the strain saturates at low frequencies (0.1 and 1 Hz) with increasing electric field amplitude. Such an effect could be plausibly attributed to voltage partitioning between the grain boundaries and grain cores of the polycrystalline ceramics [58]. The CCZ-20 does not exhibit strain saturation behavior throughout the investigated electric field range. The strain saturation and relaxation behaviors are distinctive for the 5-20 mol% RE_2O_3-doped-ceria ceramics with cubic fluorite lattice symmetry, as shown in our previous reports [224025]. From the slope of the strain vs E^2 plot in **Fig. 4a-b**, the electrostrictive strain coefficient (M_{33}) was assessed and plotted as a function of electric field frequency in **Fig. 4c**. As shown, the M_{33} value is slightly higher in the CCZ-10 sample. Furthermore, CCZ-10 shows a fairly steady M_{33} $\approx 10^{-17}$ $(m/V)^2$ up to 40 Hz, followed by a sharp relaxation. Meanwhile, CCZ-20 illustrates non-ideal Debye-type relaxation with frequencies similar to GDC-10 (10 mol% Gd-doped ceria) and SDC-10 (10 mol% Sm-doped ceria). The ratio of $M_{33}^{(1Hz)}/M_{33}^{(>100Hz)}$ is approximately 3 to 5-fold. It was demonstrated that frequency-related M_{33} relaxation is typical in RE_2O_3-doped-ceria, associated with dopant-defect pairs interaction in the crystal lattice, that responds slowly to electric field [182559]. The reported M_{33} value of 8YSZ and 3YSZ in the literature was $\approx 10^{-19}$ and $\approx 10^{-21}$ $(m/V)^2$, respectively [5455], which conforms to the Newnham empirical scaling law of classical electrostrictive materials, *i.e.*, electrostriction $|Q_h|$ coefficient ($(|Q_{ijkl}| = \frac{M_{ijkl}}{[\epsilon_0(\epsilon_r-1)]^2}, |Q_h| = Q_{ijkl} + Q_{iiii})$ where Q_{ijkl} and Q_{iiii} are transverse and longitudinal electrostriction coefficients, respectively) scales with the ratio of elastic compliance to the dielectric constant, $|Q_h| \approx 2.37(s/\epsilon_0\epsilon_r)^{0.6}$. The M_{33} value at the low-frequency regime is $>10^{-17}$ $(m/V)^2$ for both of these samples, which is equivalent to ($|Q_h| \approx 80$ m^4/C^2). This value is roughly two orders of magnitude larger than the Newnham empirical prediction (**see Fig. 4d**), is anomalously large, and represents CCZ as "giant" electrostrictors. The $|Q_h|$ (relaxed) value at the high-frequency regime is approximately ≈ 10 m^4/C^2 and above the pink-shaded area. A combination of a high electrostrictive coefficient and a small dielectric constant ($\varepsilon = 25$-30) is not usual for classical electrostrictors. We, therefore, surmise that the unusual electrostrictive activity in the CCZ compound is fundamentally very distinct from classical phenomena.

Although the exact mechanism of electrostriction in CCZ is unknown, it is highly anticipated that the mechanism is similar to that of doped ceria and bismuth oxide ceramics and ascribed to the electric-field induced rearrangement of local lattice distortions in the vicinity of the oxygen vacancies [216061]. The latter materials demonstrate anelastic behavior, such as creep at room temperature.

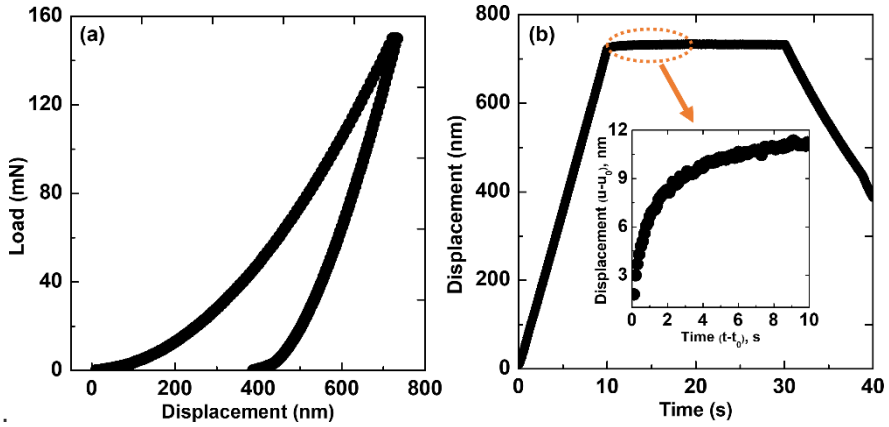

Figure 5: (a) A typical load-displacement curve during nanoindentation measurement at room temperature (b) Indenter displacement of CCZ-10 ceramics under fast loading of 15 mN/s, primary creep observed in the hold phase (dashed oval in (b)) and inset.

To verify whether the CCZ samples exhibit room-temperature creep, we performed the Nanoindentation measurement. The indentation depth was ca. 800 nm, which resembles an equivalent contact diameter of 4500 nm, i.e., manifold grains were being examined. **Fig. 5a-b** displays a typical load-displacement and displacement-time curve of the CCZ-10 sample, illustrating a primary creep at the hold phase (first 10 seconds) as a gradual increase in displacement at maximum load, evidencing viscoelastic behavior. The following empirical formula can describe the creep-driven displacement with dwelling time, $(u - u_0) = A(t - t_0)^m$, where u_0 is the initial displacement at the commencement of the hold stage t_0, A is the creep constant, and m is the fitting exponent. As projected, the A value is slightly higher in the CCZ-10 (6.7 nm/s$^{0.24}$) sample than in CCZ-20 (5.5 nm/s$^{0.14}$). Different grain boundary volumes could be the reason for the lower creep in CCZ-20 which has a larger average grain size. More importantly, the A value is lower than doped ceria ceramics (15-20 nm/s$^{0.33}$) [4562]. Such a result is expected since the creep displacement in CCZ is *ca*. 4 times lower than ceria, measured in the same experimental protocol [45]. As reported in Ref. [55], the 8YSZ single crystal does not display

any noticeable creep at room temperatures during the 10-second hold. Therefore, an analogous mechanism to doped ceria and bismuth oxide ceramics (highly oxygen defective fluorite structure), creep in CCZ can be attributed to the anisotropic mechanical stress-induced lability of cation-oxygen vacancy complex [63]. If the time scale of the applied load (fast loading) is shorter than the time required for the defect complex to reorganize, then creep deformation occurs, and the lattice continues rearranging during the hold phase. If loading is considerably slow enough for the complexes to rearrange, creep is hindered [64]. Although both the creep and electrostriction are expected to be governed by the presence of oxygen vacancies (cation-vacancy complex), there is no direct correlation between them. They differ considerably from material to material, even having the same crystal structure [21]. The mechanical properties obtained from the Vickers micro-indentation method are listed in **Table 1**.

Table 1. The measured mechanical properties *i.e.,* bending strength, fracture toughness, hardness, and Young's modulus of CCZ pellets. Each value is calculated from ca. 5 indentations and averaged.

Sample ID	**Bending Strength [MPa]**	**Fracture Toughness, K_{IC} [MPa*m$^{1/2}$]**	**Hardness, HV10 [kp]**	**Young's Modulus, E [GPa]**
CCZ-10	1020 ± 99	6.38 ± 0.02	1237 ± 10	205 ± 3
CCZ-20	346 ± 24	2.75 ± 0.08	1350 ± 14	203 ± 3.4
3Y-TZP	990 ± 130 [20]	4-6 [65]	1260 ± 30 [20]	182 ± 3 [65]
8YSZ [66]	328 ± 20	1.30 ± 0.02	1300 ± 10	~ 205
GDC-10	175 [67]	1.9-2.1 [68]	880 ± 20 [68]	180 [67]

As shown in **Table 1**, Young's modulus is identical in both samples; however, bending strength, fracture toughness, and hardness values differ between them. The CCZ-20 has a higher hardness value than the CCZ-10 sample—but has lower strength and fracture toughness than the latter. CCZ-10 has comparable properties to 3Y-TZP (sintered in similar conditions), a tetragonal high-strength zirconia material. Moreover, compared to 8YSZ and GDC-10, two cubic materials proposed for electrostrictors, both the strength and fracture toughness of CCZ-20 are considerably higher, probably due to the remaining fraction of the tetragonal phase. As an electromechanical device is operated under dynamic loading conditions besides electromechanical performance, high mechanical strength, especially fatigue strength, is required. Fatigue strength can be estimated from bending strength and the K_{I0}/K_{IC} ratio (K_{IC} = 6

MPa√m, K_{IO} typically 4 MPa√m for TZP [69]). Therefore, CCZ-10 has a fatigue strength of 650 MPa. In predominantly cubic CCZ-20, where little R-curve behavior is expected ($K_{IO}/K_{IC} \rightarrow 1$), fatigue strength is closer to the measured bending strength (~250 MPa).

Conclusions

In this work, two compositions of compositionally complex zirconia-based oxides were fabricated by hot pressing at 1350 °C and are partially stabilized. In the CCZ-10 sample, micron-sized cubic grains are embedded in a matrix of tetragonal grains, and CCZ-20 vice versa. The CCZ-10 sample demonstrates a higher fracture toughness and bending strength than the CCZ-20 sample. Remarkably, both samples reveal room-temperature mechanical creep (anelasticity) and nonclassical electromechanical responses like oxygen defective ceria and bismuth oxide-based compounds. The electrostriction follows typical strain relaxation effects with frequencies, which is directed by the presence of the (weak) dopant-defect interaction in the lattice system. Based on the Newnham scaling law, the electromechanical response is nonclassical and exceeds the values by more than two orders of magnitude. To sum up, compositionally complex zirconia ceramics represent another member of fluorite-structured or fluorite structure-derived nonclassical ionic electrostictors, fundamentally different from the classical electromechanically active ceramics materials.

Acknowledgments

This research was supported by the PRIME program of the German Academic Exchange Service (DAAD) with funds from the German Federal Ministry of Education and Research (BMBF) and the DEMETRA M.ERA-NET project reference number: project10098 (NCN project number 2022/04/Y/ST5/00165).

References

(1) Rost, C. M.; Sachet, E.; Borman, T.; Moballegh, A.; Dickey, E. C.; Hou, D.; Jones, J. L.; Curtarolo, S.; Maria, J. P. Entropy-Stabilized Oxides. *Nat Commun* **2015**, *6*. https://doi.org/10.1038/ncomms9485.

(2) Chen, K.; Pei, X.; Tang, L.; Cheng, H.; Li, Z.; Li, C.; Zhang, X.; An, L. A Five-Component Entropy-Stabilized Fluorite Oxide. *J Eur Ceram Soc* **2018**, *38* (11), 4161–4164. https://doi.org/10.1016/j.jeurceramsoc.2018.04.063.

(3) Yeh, J. -W.; Chen, S. -K.; Lin, S. -J.; Gan, J. -Y.; Chin, T. -S.; Shun, T. -T.; Tsau, C. -H.; Chang, S. -Y. Nanostructured High-Entropy Alloys with Multiple Principal Elements: Novel Alloy Design Concepts and Outcomes. *Adv Eng Mater* **2004**, *6* (5), 299–303. https://doi.org/10.1002/adem.200300567.

(4) Aamlid, S. S.; Oudah, M.; Rottler, J.; Hallas, A. M. Understanding the Role of Entropy in High Entropy Oxides. *J Am Chem Soc* **2023**, *145* (11), 5991–6006. https://doi.org/10.1021/jacs.2c11608.

(5) Gager, E.; Nino, J. C. Processing, Phase Stability, and Conductivity of Multication-Doped Ceria. *Inorganics (Basel)* **2023**, *11* (7), 299. https://doi.org/10.3390/inorganics11070299.

(6) Wright, A. J.; Wang, Q.; Huang, C.; Nieto, A.; Chen, R.; Luo, J. From High-Entropy Ceramics to Compositionally-Complex Ceramics: A Case Study of Fluorite Oxides. *J Eur Ceram Soc* **2020**, *40* (5), 2120–2129. https://doi.org/10.1016/j.jeurceramsoc.2020.01.015.

(7) Brahlek, M.; Gazda, M.; Keppens, V.; Mazza, A. R.; McCormack, S. J.; Mielewczyk-Gryń, A.; Musico, B.; Page, K.; Rost, C. M.; Sinnott, S. B.; Toher, C.; Ward, T. Z.; Yamamoto, A. What Is in a Name: Defining "High Entropy" Oxides. *APL Mater* **2022**, *10* (11). https://doi.org/10.1063/5.0122727.

(8) Gild, J.; Samiee, M.; Braun, J. L.; Harrington, T.; Vega, H.; Hopkins, P. E.; Vecchio, K.; Luo, J. High-Entropy Fluorite Oxides. *J Eur Ceram Soc* **2018**, *38* (10), 3578–3584. https://doi.org/10.1016/j.jeurceramsoc.2018.04.010.

(9) Kamecki, B.; Karczewski, J.; Cempura, G.; Jasiński, P.; Molin, S. Evaluation of Structural and Electrical Properties of Multicomponent Spinel Oxide Thin Films Deposited via Spray Pyrolysis Technique. *Mater Charact* **2023**, *203*, 113097. https://doi.org/10.1016/j.matchar.2023.113097.

(10) Banerjee, R.; Chatterjee, S.; Ranjan, M.; Bhattacharya, T.; Mukherjee, S.; Jana, S. S.; Dwivedi, A.; Maiti, T. High-Entropy Perovskites: An Emergent Class of Oxide Thermoelectrics with Ultralow Thermal Conductivity. *ACS Sustain Chem Eng* **2020**, *8* (46), 17022–17032. https://doi.org/10.1021/acssuschemeng.0c03849.

(11) Sukkurji, P. A.; Cui, Y.; Lee, S.; Wang, K.; Azmi, R.; Sarkar, A.; Indris, S.; Bhattacharya, S. S.; Kruk, R.; Hahn, H.; Wang, Q.; Botros, M.; Breitung, B. Mechanochemical Synthesis of Novel Rutile-Type High Entropy Fluorides for Electrocatalysis. *J Mater Chem A Mater* **2021**, *9* (14), 8998–9009. https://doi.org/10.1039/D0TA10209A.

(12) Teng, Z.; Zhu, L.; Tan, Y.; Zeng, S.; Xia, Y.; Wang, Y.; Zhang, H. Synthesis and Structures of High-Entropy Pyrochlore Oxides. *J Eur Ceram Soc* **2020**, *40* (4), 1639–1643. https://doi.org/10.1016/j.jeurceramsoc.2019.12.008.

(13) Sarkar, A.; Djenadic, R.; Usharani, N. J.; Sanghvi, K. P.; Chakravadhanula, V. S. K.; Gandhi, A. S.; Hahn, H.; Bhattacharya, S. S. Nanocrystalline Multicomponent Entropy Stabilised Transition Metal Oxides. *J Eur Ceram Soc* **2017**, *37* (2), 747–754. https://doi.org/10.1016/j.jeurceramsoc.2016.09.018.

(14) Biesuz, M.; Chen, J.; Bortolotti, M.; Speranza, G.; Esposito, V.; Sglavo, V. M. Ni-Free High-Entropy Rock Salt Oxides with Li Superionic Conductivity. *J Mater Chem A Mater* **2022**, *10* (44), 23603–23616. https://doi.org/10.1039/D2TA06101E.

(15) Schmitt, R.; Nenning, A.; Kraynis, O.; Korobko, R.; Frenkel, A. I.; Lubomirsky, I.; Haile, S. M.; Rupp, J. L. M. A Review of Defect Structure and Chemistry in Ceria and Its Solid Solutions. *Chem Soc Rev* **2020**, *49* (2), 554–592. https://doi.org/10.1039/C9CS00588A.

(16) Esposito, V.; Traversa, E. Design of Electroceramics for Solid Oxides Fuel Cell Applications: Playing with Ceria. *Journal of the American Ceramic Society* **2008**, *91* (4), 1037–1051. https://doi.org/10.1111/j.1551-2916.2008.02347.x.

(17) Coduri, M.; Checchia, S.; Longhi, M.; Ceresoli, D.; Scavini, M. Rare Earth Doped Ceria: The Complex Connection Between Structure and Properties. *Front Chem* **2018**, *6*. https://doi.org/10.3389/fchem.2018.00526.

(18) Kabir, A.; Buratto Tinti, V.; Varenik, M.; Lubomirsky, I.; Esposito, V. Electromechanical Dopant–Defect Interaction in Acceptor-Doped Ceria. *Mater Adv* **2020**, *1* (8), 2717–2720. https://doi.org/10.1039/D0MA00563K.

(19) Xu, L.; Wang, H.; Su, L.; Lu, D.; Peng, K.; Gao, H. A New Class of High-Entropy Fluorite Oxides with Tunable Expansion Coefficients, Low Thermal Conductivity and Exceptional Sintering Resistance. *J Eur Ceram Soc* **2021**, *41* (13), 6670–6676. https://doi.org/10.1016/j.jeurceramsoc.2021.05.043.

(20) Kern, F.; Gadow, R.; Kabir, A. Mechanical Properties and Low Temperature Degradation Resistance of Alumina-Doped 3Y-TZP Fabricated from Stabilizer Coated Powders Mechanical Properties and Low Temperature Degradation Resistance of Alumina-Doped 3Y-TZP Fabricated from Stabilizer Coated Powders WŁAŚCIWOŚCI MECHANICZNE I ODPORNOŚĆ NA NISKOTEMPERATUROWĄ DEGRADACJĘ DOMIESZKOWANEGO TLENKIEM GLINU 3Y-TZP, WYTWORZONEGO Z PROSZKÓW POKRYWANYCH STABILIZATOREM. **1984**, *69*, 279–285.

(21) Wachtel, E.; Frenkel, A. I.; Lubomirsky, I. Anelastic and Electromechanical Properties of Doped and Reduced Ceria. *Advanced Materials* **2018**, *30* (41), 1707455. https://doi.org/10.1002/adma.201707455.

(22) Zhang, H.; Vasiljevic, M.; Bergne, A.; Park, D.; Insinga, A. R.; Yun, S.; Esposito, V.; Pryds, N. Engineering of Electromechanical Oxides by Symmetry Breaking. *Adv Mater Interfaces* **2023**, *10* (18). https://doi.org/10.1002/admi.202300083.

(23) Zhang, H.; Pryds, N.; Park, D.-S.; Gauquelin, N.; Santucci, S.; Christensen, D. V.; Jannis, D.; Chezganov, D.; Rata, D. A.; Insinga, A. R.; Castelli, I. E.; Verbeeck, J.; Lubomirsky, I.; Muralt, P.; Damjanovic, D.; Esposito, V. Atomically Engineered Interfaces Yield Extraordinary Electrostriction. *Nature* **2022**, *609* (7928), 695–700. https://doi.org/10.1038/s41586-022-05073-6.

(24) Kabir, A.; Santucci, S.; Van Nong, N.; Varenik, M.; Lubomirsky, I.; Nigon, R.; Muralt, P.; Esposito, V. Effect of Oxygen Defects Blocking Barriers on Gadolinium Doped Ceria (GDC) Electro-Chemo-Mechanical Properties. *Acta Mater* **2019**, *174*, 53–60. https://doi.org/10.1016/j.actamat.2019.05.009.

(25) Varenik, M.; Nino, J. C.; Wachtel, E.; Kim, S.; Yeheskel, O.; Yavo, N.; Lubomirsky, I. Dopant Concentration Controls Quasi-Static Electrostrictive Strain Response of Ceria Ceramics. *ACS Appl Mater Interfaces* **2020**, *12* (35), 39381–39387. https://doi.org/10.1021/acsami.0c07799.

(26) Cheng, F.; Zhang, F.; Liu, Y.; Guo, M.; Cheng, C.; Hou, J.; Miao, Y.; Gao, F.; Wang, X. Ti4+-Incorporated Fluorite-Structured High-Entropy Oxide (Ce,Hf,Y,Pr,Gd)O2−δ: Optimizing Preparation and CMAS Corrosion Behavior. *Journal of Advanced Ceramics* **2022**, *11* (11), 1801–1814. https://doi.org/10.1007/s40145-022-0649-4.

(27) Chen, K.; Pei, X.; Tang, L.; Cheng, H.; Li, Z.; Li, C.; Zhang, X.; An, L. A Five-Component Entropy-Stabilized Fluorite Oxide. *J Eur Ceram Soc* **2018**, *38* (11), 4161–4164. https://doi.org/10.1016/j.jeurceramsoc.2018.04.063.

(28) Wright, A. J.; Wang, Q.; Huang, C.; Nieto, A.; Chen, R.; Luo, J. From High-Entropy Ceramics to Compositionally-Complex Ceramics: A Case Study of Fluorite Oxides. *J Eur Ceram Soc* **2020**, *40* (5), 2120–2129. https://doi.org/10.1016/j.jeurceramsoc.2020.01.015.

(29) Zhu, M.; Yi, L.; Zhou, R.; Du, C.; Tian, C.; Yang, J. Microstructural, Electrical and Thermal Characterization of Dy3+, Sm3+, Er3+, Y3+ and Gd3+ Multi-Doped Cerium Dioxide as SOFCs Solid Electrolytes. *J Alloys Compd* **2024**, *976*, 173108. https://doi.org/10.1016/j.jallcom.2023.173108.

(30) Spiridigliozzi, L.; Ferone, C.; Cioffi, R.; Accardo, G.; Frattini, D.; Dell'Agli, G. Entropy-Stabilized Oxides Owning Fluorite Structure Obtained by Hydrothermal Treatment. *Materials* **2020**, *13* (3), 558. https://doi.org/10.3390/ma13030558.

(31) Spiridigliozzi, L.; Dell'Agli, G.; Esposito, S.; Rivolo, P.; Grasso, S.; Sglavo, V. M.; Biesuz, M. Ultra-Fast High-Temperature Sintering (UHS) of Ce0.2Zr0.2Y0.2Gd0.2La0.2O2−δ Fluorite-Structured Entropy-Stabilized Oxide (F-ESO). *Scr Mater* **2022**, *214*, 114655. https://doi.org/10.1016/j.scriptamat.2022.114655.

(32) Ye, F.; Meng, F.; Luo, T.; Qi, H. Ultrafast High-Temperature Sintering of (Y0.2Dy0.2Er0.2Tm0.2Yb0.2)4Hf3O12 High-Entropy Ceramics with Defective Fluorite Structure. *J Eur Ceram Soc* **2022**, *42* (11), 4686–4691. https://doi.org/10.1016/j.jeurceramsoc.2022.04.023.

(33) Djenadic, R.; Sarkar, A.; Clemens, O.; Loho, C.; Botros, M.; Chakravadhanula, V. S. K.; Kübel, C.; Bhattacharya, S. S.; Gandhi, A. S.; Hahn, H. Multicomponent Equiatomic Rare Earth Oxides. *Mater Res Lett* **2017**, *5* (2), 102–109. https://doi.org/10.1080/21663831.2016.1220433.

(34) Sarkar, A.; Loho, C.; Velasco, L.; Thomas, T.; Bhattacharya, S. S.; Hahn, H.; Djenadic, R. Multicomponent Equiatomic Rare Earth Oxides with a Narrow Band Gap and Associated Praseodymium Multivalency. *Dalton Transactions* **2017**, *46* (36), 12167–12176. https://doi.org/10.1039/C7DT02077E.

(35) Chen, K.; Ma, J.; Tan, C.; Li, C.; An, L. An Anion-Deficient High-Entropy Fluorite Oxide with Very Low Density. *Ceram Int* **2021**, *47* (15), 21207–21211. https://doi.org/10.1016/j.ceramint.2021.04.123.

(36) Brahlek, M.; Gazda, M.; Keppens, V.; Mazza, A. R.; McCormack, S. J.; Mielewczyk-Gryń, A.; Musico, B.; Page, K.; Rost, C. M.; Sinnott, S. B.; Toher, C.; Ward, T. Z.; Yamamoto, A. What Is in a

Name: Defining “High Entropy” Oxides. *APL Mater* **2022**, *10* (11). https://doi.org/10.1063/5.0122727.

(37) Chen, K.; Pei, X.; Tang, L.; Cheng, H.; Li, Z.; Li, C.; Zhang, X.; An, L. A Five-Component Entropy-Stabilized Fluorite Oxide. *J Eur Ceram Soc* **2018**, *38* (11), 4161–4164. https://doi.org/10.1016/j.jeurceramsoc.2018.04.063.

(38) Tinti, V. B.; Kabir, A.; Han, J. K.; Molin, S.; Esposito, V. Gigantic Electro-Chemo-Mechanical Properties of Nanostructured Praseodymium Doped Ceria. *Nanoscale* **2021**, *13* (16), 7583–7589. https://doi.org/10.1039/D1NR00601K.

(39) Koettgen, J.; Grieshammer, S.; Hein, P.; Grope, B. O. H.; Nakayama, M.; Martin, M. Understanding the Ionic Conductivity Maximum in Doped Ceria: Trapping and Blocking. *Physical Chemistry Chemical Physics* **2018**, *20* (21), 14291–14321. https://doi.org/10.1039/C7CP08535D.

(40) Kabir, A.; Bowen, J. R.; Varenik, M.; Lubomirsky, I.; Esposito, V. Enhanced Electromechanical Response in Sm and Nd Co-Doped Ceria. *Materialia (Oxf)* **2020**, *12*, 100728. https://doi.org/10.1016/j.mtla.2020.100728.

(41) Dąbrowa, J.; Szymczak, M.; Zajusz, M.; Mikuła, A.; Moździerz, M.; Berent, K.; Wytrwal-Sarna, M.; Bernasik, A.; Stygar, M.; Świerczek, K. Stabilizing Fluorite Structure in Ceria-Based High-Entropy Oxides: Influence of Mo Addition on Crystal Structure and Transport Properties. *J Eur Ceram Soc* **2020**, *40* (15), 5870–5881. https://doi.org/10.1016/j.jeurceramsoc.2020.07.014.

(42) Zhang, H.; Castelli, I. E.; Santucci, S.; Sanna, S.; Pryds, N.; Esposito, V. Atomic-Scale Insights into Electro-Steric Substitutional Chemistry of Cerium Oxide. *Physical Chemistry Chemical Physics* **2020**, *22* (38), 21900–21908. https://doi.org/10.1039/D0CP03298K.

(43) MENDELSON, M. I. Average Grain Size in Polycrystalline Ceramics. *Journal of the American Ceramic Society* **1969**, *52* (8), 443–446. https://doi.org/10.1111/j.1151-2916.1969.tb11975.x.

(44) Merk, A.-L.; Kern, F. Influence of Starting Powder Choice on Structure Property Relations in Gadolinia Stabilized Zirconia 3Gd-TZP Manufactured from Co-Milled Starting Powders. *J Eur Ceram Soc* **2021**, *41* (15), 7783–7791. https://doi.org/10.1016/j.jeurceramsoc.2021.08.002.

(45) Kabir, A.; Espineira-Cachaza, M.; Fiordaliso, E. M.; Ke, D.; Grasso, S.; Merle, B.; Esposito, V. Effect of Cold Sintering Process (CSP) on the Electro-Chemo-Mechanical Properties of Gd-Doped Ceria (GDC). *J Eur Ceram Soc* **2020**, *40* (15), 5612–5618. https://doi.org/10.1016/j.jeurceramsoc.2020.06.010.

(46) Gazzoli, D.; Mattei, G.; Valigi, M. Raman and X-Ray Investigations of the Incorporation of Ca2+ and Cd2+ in the ZrO2 Structure. *Journal of Raman Spectroscopy* **2007**, *38* (7), 824–831. https://doi.org/10.1002/jrs.1708.

(47) Bersani, D.; Lottici, P. P.; Rangel, G.; Ramos, E.; Pecchi, G.; Gómez, R.; López, T. Micro-Raman Study of Indium Doped Zirconia Obtained by Sol–Gel. *J Non Cryst Solids* **2004**, *345–346*, 116–119. https://doi.org/10.1016/j.jnoncrysol.2004.08.006.

(48) Strasberg, M.; Barrett, A. A.; Anusavice, K. J.; Mecholsky, J. J.; Nino, J. C. Influence of Roughness on the Efficacy of Grazing Incidence X-Ray Diffraction to Characterize Grinding-Induced Phase

Changes in Yttria-Tetragonal Zirconia Polycrystals (Y-TZP). *J Mater Sci* **2014**, *49* (4), 1630–1638. https://doi.org/10.1007/s10853-013-7846-z.

(49) Kern, F. Ytterbia–Neodymia–Costabilized TZP—Breaking the Limits of Strength–Toughness Correlations for Zirconia? *J Eur Ceram Soc* **2013**, *33* (5), 965–973. https://doi.org/10.1016/j.jeurceramsoc.2012.10.028.

(50) Kern, F. High Toughness and Strength in Yttria–Neodymia Costabilized Zirconia Ceramics. *Scr Mater* **2012**, *67* (3), 301–304. https://doi.org/10.1016/j.scriptamat.2012.05.009.

(51) KERN, F.; GADOW, R. Tough to Brittle Transition with Increasing Grain Size in 3Yb-TZP Ceramics Manufactured from Stabilizer Coated Nanopowder. *Journal of the Ceramic Society of Japan* **2016**, *124* (10), 1083–1089. https://doi.org/10.2109/jcersj2.16106.

(52) Ahamer, C.; Opitz, A. K.; Rupp, G. M.; Fleig, J. Revisiting the Temperature Dependent Ionic Conductivity of Yttria Stabilized Zirconia (YSZ). *J Electrochem Soc* **2017**, *164* (7), F790–F803. https://doi.org/10.1149/2.0641707jes.

(53) Varenik, M.; Nino, J. C.; Wachtel, E.; Kim, S.; Cohen, S. R.; Lubomirsky, I. Trivalent Dopant Size Influences Electrostrictive Strain in Ceria Solid Solutions. *ACS Appl Mater Interfaces* **2021**, *13* (17), 20269–20276. https://doi.org/10.1021/acsami.0c20810.

(54) Yimnirun, R.; Moses, P. J.; Newnham, R. E.; Meyer, J. R. J. Electrostrictive Strain in Low-Permittivity Dielectrics. *J Electroceram* **2002**, *8* (2), 87–98. https://doi.org/10.1023/A:1020543610685.

(55) Yavo, N.; Smith, A. D.; Yeheskel, O.; Cohen, S.; Korobko, R.; Wachtel, E.; Slater, P. R.; Lubomirsky, I. Large Nonclassical Electrostriction in (Y, Nb)-Stabilized δ -Bi_2O_3. *Adv Funct Mater* **2016**, *26* (7), 1138–1142. https://doi.org/10.1002/adfm.201503942.

(56) Yu, J.; Janolin, P.-E. Defining “Giant” Electrostriction. *J Appl Phys* **2022**, *131* (17), 170701. https://doi.org/10.1063/5.0079510.

(57) Newnham, R. E.; Sundar, V.; Yimnirun, R.; Su, J.; Zhang, Q. M. Electrostriction: Nonlinear Electromechanical Coupling in Solid Dielectrics. *J Phys Chem B* **1997**, *101* (48), 10141–10150. https://doi.org/10.1021/jp971522c.

(58) Yavo, N.; Yeheskel, O.; Wachtel, E.; Ehre, D.; Frenkel, A. I.; Lubomirsky, I. Relaxation and Saturation of Electrostriction in 10 Mol% Gd-Doped Ceria Ceramics. *Acta Mater* **2018**, *144*, 411–418. https://doi.org/10.1016/j.actamat.2017.10.056.

(59) Korobko, R.; Lerner, A.; Li, Y.; Wachtel, E.; Frenkel, A. I.; Lubomirsky, I. In-Situ Extended X-Ray Absorption Fine Structure Study of Electrostriction in Gd Doped Ceria. *Appl Phys Lett* **2015**, *106* (4), 042904. https://doi.org/10.1063/1.4906857.

(60) Li, Y.; Kraynis, O.; Kas, J.; Weng, T.-C.; Sokaras, D.; Zacharowicz, R.; Lubomirsky, I.; Frenkel, A. I. Geometry of Electromechanically Active Structures in Gadolinium - Doped Cerium Oxides. *AIP Adv* **2016**, *6* (5). https://doi.org/10.1063/1.4952645.

(61) Korobko, R.; Patlolla, A.; Kossoy, A.; Wachtel, E.; Tuller, H. L.; Frenkel, A. I.; Lubomirsky, I. Giant Electrostriction in Gd-Doped Ceria. *Advanced Materials* **2012**, *24* (43), 5857–5861. https://doi.org/10.1002/adma.201202270.

(62) Kabir, A.; Kyu Han, J.; Merle, B.; Esposito, V. The Role of Oxygen Defects on the Electro-Chemo-Mechanical Properties of Highly Defective Gadolinium Doped Ceria. *Mater Lett* **2020**, *266*, 127490. https://doi.org/10.1016/j.matlet.2020.127490.

(63) Korobko, R.; Kim, S. K.; Kim, S.; Cohen, S. R.; Wachtel, E.; Lubomirsky, I. The Role of Point Defects in the Mechanical Behavior of Doped Ceria Probed by Nanoindentation. *Adv Funct Mater* **2013**. https://doi.org/10.1002/adfm.201301536.

(64) Varenik, M.; Cohen, S.; Wachtel, E.; Frenkel, A. I.; Nino, J. C.; Lubomirsky, I. Oxygen Vacancy Ordering and Viscoelastic Mechanical Properties of Doped Ceria Ceramics. *Scr Mater* **2019**, *163*, 19–23. https://doi.org/10.1016/j.scriptamat.2018.12.024.

(65) Eichler, J.; Hoffman, M.; Eisele, U.; Rödel, J. R-Curve Behaviour of 2Y-TZP with Submicron Grain Size. *J Eur Ceram Soc* **2006**, *26* (16), 3575–3582. https://doi.org/10.1016/j.jeurceramsoc.2005.11.012.

(66) Chen, P.; Li, X.; Tian, F.; Liu, Z.; Hu, D.; Xie, T.; Liu, Q.; Li, J. Fabrication, Microstructure, and Properties of 8 Mol% Yttria-Stabilized Zirconia (8YSZ) Transparent Ceramics. *Journal of Advanced Ceramics* **2022**, *11* (7), 1153–1162. https://doi.org/10.1007/s40145-022-0602-6.

(67) Yasuda, K.; Uemura, K.; Shiota, T. Sintering and Mechanical Properties of Gadolinium-Doped Ceria Ceramics. *J Phys Conf Ser* **2012**, *339* (1), 012006. https://doi.org/10.1088/1742-6596/339/1/012006.

(68) Mangalaraja, R. V.; Ananthakumar, S.; Uma, K.; Jiménez, R. M.; López, M.; Camurri, C. P. Microhardness and Fracture Toughness of Ce0.9Gd0.1O1.95 for Manufacturing Solid Oxide Electrolytes. *Materials Science and Engineering: A* **2009**, *517* (1–2), 91–96. https://doi.org/10.1016/j.msea.2009.03.046.

(69) Chevalier, J.; Olagnon, C.; Fantozzi, G.; Cales, B. Subcritical Crack Growth and Thresholds in a 3Y-TZP Ceramic under Static and Cyclic Loading Conditions. *Ceram Int* **1997**, *23* (3), 263–266. https://doi.org/10.1016/S0272-8842(96)00037-5.